AIMS Mathematics

https://www.aimspress.com/journal/Math

AIMS Mathematics, 11(8): 27056–27084.
DOI:10.3934/math.20261084
Received: 26 May 2026
Revised: 11 August 2026
Accepted: 18 August 2026
Published: 27 August 2026

Research article

A fourth-order compact functional-calculus method for distributed-order spectral diffusion

Xiaotong Li and Jianxin Li*

Department of Basic Education, Xinjiang University of Political Science and Law, Tumushuke 843900, China

* **Correspondence:** Email: 2021302@xjzfu.edu.cn; Tel: +86-18135900624.

Abstract: We studied a full-spectral distributed-order diffusion equation on a rectangular domain with homogeneous Dirichlet boundary conditions, driven by a nonnegative integrable order-density function that represents a continuum of spatial scaling contributions. The order superposition was represented by the equation $\varphi(s) = \int_{\mu^-}^{\mu^+} \rho(\mu) s^{\mu/2}\, \mathrm{d}\mu$ and our objective was to construct and analyze a fourth-order discretization that preserves this spectral structure while admitting an efficient sine-modal implementation. We discretized the positive Dirichlet Laplacian by the fourth-order compact Kronecker-sum operator $A^{(4)}_{\Delta,h} = I_y \otimes A^{(4)}_{x,h} + A^{(4)}_{y,h} \otimes I_x$, defined $\Phi_h = \varphi(A^{(4)}_{\Delta,h})$, and used the dissipative generator $L_h = -\Phi_h$. The main consistency result showed that the compact eigenvalue perturbation is preserved under the distributed-order functional calculus, yielding a fourth-order discrete L^2 approximation to $\varphi(-\Delta_D)$ after grid restriction. An unsplit modal Crank–Nicolson scheme was then obtained by diagonalizing Φ_h with the discrete sine transform, where the positivity of the exact symbol or the positive quadrature symbol gives unconditional discrete L^2 stability. Under the stated regularity assumptions, the fully discrete error is $O(\tau^2 + h^4)$ for the exact-symbol scheme and $O(\tau^2 + h^4 + E_\mu)$ for its positive-quadrature version. The numerical experiments were consistent with the proved fourth-order spatial accuracy, second-order temporal accuracy, and unconditional stability, and they also illustrated quadrature sensitivity, implementation scaling, and the accuracy gain over the second-order full-spectral counterpart.

Keywords: distributed-order diffusion; spectral fractional operator; compact finite difference; matrix functional calculus; Crank–Nicolson method; stability and convergence
Mathematics Subject Classification: 35R11, 65M06, 65M12, 65M15, 65R20

1. Introduction

Distributed-order diffusion models describe transport processes in which a continuum of fractional orders contributes to the effective dynamics [1–3]. Such models arise in anomalous diffusion, viscoelasticity, and heterogeneous media, and have been studied both analytically and numerically [4, 5]. Numerical methods for distributed-order equations typically combine a spatial discretization with a quadrature rule for the order integral [6–9]. Matrix functional calculus provides a natural framework for discretized fractional elliptic operators and spectral fractional Laplacians [10–12].

This paper considers a spatial spectral distributed-order diffusion equation of the form

$$u_t = -\varphi(B)u + f, \qquad B = -\Delta_D,$$

on a rectangular domain with homogeneous Dirichlet boundary conditions. The scalar symbol φ represents a nonnegative superposition of powers of the positive Dirichlet Laplacian. The numerical question addressed here is whether the continuous operator B can be replaced, inside $\varphi(\cdot)$, by a fourth-order compact finite-difference generator while retaining high-order consistency, positivity, and a sine-modal implementation.

Compact finite differences are a classical way to obtain high-order spatial resolution [13, 14]. For spectral fractional diffusion, however, the discretization is not only an approximation of the Laplacian; it is also the argument of a nonlocal matrix function. This makes the transfer from a compact generator to a compact approximation of $\varphi(B)$ a separate issue. On rectangular Dirichlet domains, the compact Kronecker-sum generator $A^{(4)}_{\Delta,h}$ is diagonalizable by the discrete sine transform, so the full two-dimensional symbol can be evaluated mode by mode as $\varphi(\mathcal{A}^{(4)}_{mn,h})$. This differs from directional factorizations used in classical alternating direction implicit (ADI) methods [15–17] and in several fractional or distributed-order schemes [18, 19].

Several related directions should be distinguished. Recent high-order spectral studies include time-fractional diffusion on semi-infinite domains, multidimensional diffusion with third-kind boundary conditions, and polynomial tau formulations for time-fractional diffusion [20–23]; related shifted-Lucas collocation work addresses fractional dynamical systems [24]. Compact matrix transfer and discrete sine transform (DST) implementations have been developed for fixed-order spectral fractional Laplacians [25], and fourth-order compact matrix-transfer ideas have also appeared in time-space fractional reaction-diffusion computations [26]. Distributed-order space-fractional problems have been treated through quadrature and matrix-transfer techniques [27]. High-order or Crank–Nicolson alternating direction implicit (CN-ADI) methods are available for distributed-order Riesz models [19, 28, 29], but Riesz-type and spectral fractional Laplacians have different operators on bounded domains [12]. Compared with these recent compact methods, the present method places the compact two-dimensional Dirichlet generator inside a spatial distributed-order symbol and proves that the fourth-order perturbation is retained uniformly over the order interval. Compared with the distributed-order Riesz schemes, it treats the spectral fractional Laplacian and uses an unsplit DST–Crank–Nicolson update, with the quadrature error E_μ, defined in Section 4.1, kept separate. Together, these features retain fourth-order spatial accuracy across the order integral while providing an $O(N_{\mathrm{dof}} \log N_{\mathrm{dof}})$ unsplit modal update, unconditional discrete L^2 stability, and an explicit error bound $O(\tau^2 + h^4 + E_\mu)$. Here N_{dof} denotes the number of spatial degrees of freedom.

In addition to the second-order full-spectral finite-difference counterpart, a fourth-order noncompact comparator with matched settings is considered. General matrix-function solvers apply to broader matrices, whereas the rectangular Dirichlet setting considered here permits a direct DST diagonalization.

For the spatial formulation considered here, the order interval $[\mu^-, \mu^+]$ and density $\rho(\mu)$ control the wavenumber-dependent damping of the Dirichlet modes. This provides a modeling mechanism for anomalous transport in heterogeneous media with multiple spatial scaling regimes rather than a single fixed spatial order [4,5]. On rectangular domains with homogeneous Dirichlet data, the DST realization avoids dense matrix functions and supports repeated forward simulations for prescribed-order intervals and densities. Complementary studies in applied mathematics have examined nonlinear vibration suppression and active control in coupled beams, motorcycle models, electromagnetic suspension systems, and parametrically excited cantilevers [30–33].

The contributions are as follows.

(i) We construct a compact functional-calculus approximation to the full-spectral distributed-order operator $\varphi(B)$ by applying φ to $A^{(4)}_{\Delta,h} = I_y \otimes A^{(4)}_{x,h} + A^{(4)}_{y,h} \otimes I_x$.

(ii) We prove a transfer estimate showing that the compact eigenvalue perturbation remains fourth order after applying the fractional/distributed-order functional calculus.

(iii) We derive an unsplit modal Crank–Nicolson scheme and prove unconditional discrete L^2 stability for the exact symbol and for positive quadrature rules applied to the order integral.

(iv) We establish a fully discrete error estimate with second-order temporal accuracy, fourth-order spatial accuracy, and an explicit order-quadrature budget E_μ.

(v) We assess the theory through operator-level, fully discrete, temporal, order-interval, quadrature, and stability experiments, together with implementation scaling diagnostics and a comparison with a second-order full-spectral counterpart.

The rest of the paper is organized as follows. Section 2 introduces the full-spectral distributed-order model. Section 3 constructs the compact generator and proves the functional-calculus transfer estimate. Section 4 gives the unsplit modal CN method and its implementation. Section 5 proves stability and convergence. Section 6 reports numerical experiments, and Section 7 concludes.

2. Spectral distributed-order model

Let $\Omega = (0, L_x)\times(0, L_y)$ and let $B = -\Delta_D$ be the positive Dirichlet Laplacian on $L^2(\Omega)$. Its normalized eigenfunctions are

$$e_{mn}(x, y) = e^x_m(x)e^y_n(y),$$

$$e^x_m(x) = \sqrt{\frac{2}{L_x}} \sin \frac{m\pi x}{L_x}, \quad e^y_n(y) = \sqrt{\frac{2}{L_y}} \sin \frac{n\pi y}{L_y},$$

with eigenvalues

$$\Lambda_{mn} = \kappa^2_{m,x} + \kappa^2_{n,y}, \qquad \kappa_{m,x} = \frac{m\pi}{L_x}, \quad \kappa_{n,y} = \frac{n\pi}{L_y}.$$

The scalar-order superposition used here follows the classical distributed-order formulation [1, 2, 34]. We apply this superposition to the spectral spatial operator. Spectral realizations of fractional diffusion operators based on Dirichlet eigenpairs are standard in space-fractional diffusion models [11,12,35]. Nonnegative weights are standard in distributed-order models and their quadrature discretizations [3,6] and the Bernstein-function viewpoint provides the positivity background used in the functional calculus [36].

Assumption 1. *The order interval and density satisfy*

$$0 < \mu^- < \mu^+ \le 2, \qquad \rho \in L^1([\mu^-,\mu^+]), \qquad \rho(\mu) \ge 0 \textit{ for a.e. } \mu, \qquad \int_{\mu^-}^{\mu^+} \rho(\mu)\,\mathrm{d}\mu > 0.$$

The distributed-order symbol is

$$\varphi(s) = \int_{\mu^-}^{\mu^+} \rho(\mu) s^{\mu/2}\,\mathrm{d}\mu, \qquad s > 0. \tag{2.1}$$

For $0 < s \le 1$, $0 \le s^{\mu/2} \le s^{\mu^-/2} \to 0$ uniformly for $\mu \in [\mu^-,\mu^+]$ as $s \to 0^+$. Consequently, $0 \le \varphi(s) \le \|\rho\|_{L^1} s^{\mu^-/2} \to 0$, so φ extends continuously to $s = 0$ by setting $\varphi(0) = 0$. Under Assumption 1, $\varphi(s) > 0$ for $s > 0$. Since s^α is a Bernstein function for $0 < \alpha \le 1$, the nonnegative superposition in (2.1) preserves positivity under the spectral functional calculus for positive self-adjoint operators and, later, for symmetric positive definite matrices. For the continuous spectrum, $s \ge \Lambda_{11} > 0$, and Assumption 1 implies

$$\varphi(s) \le C s^{\mu^+/2}, \qquad s \ge \Lambda_{11},$$

with C independent of the modal indices.

Define $\Phi = \varphi(B)$ by spectral calculus and set $L = -\Phi$. Thus, for

$$v = \sum_{m,n\ge1} v_{mn} e_{mn}, \qquad \sum_{m,n\ge1} \varphi(\Lambda_{mn})^2 |v_{mn}|^2 < \infty,$$

we have

$$\Phi v = \sum_{m,n\ge1} \varphi(\Lambda_{mn}) v_{mn} e_{mn}, \qquad Lv = -\sum_{m,n\ge1} \varphi(\Lambda_{mn}) v_{mn} e_{mn}.$$

For $s \ge 0$, define

$$D(B^s) = \left\{ v = \sum_{m,n\ge1} v_{mn} e_{mn} : \sum_{m,n\ge1} \Lambda_{mn}^{2s} |v_{mn}|^2 < \infty \right\}.$$

Since $\Lambda_{11} > 0$, we use the equivalent graph norm

$$\|v\|_{D(B^s)}^2 = \sum_{m,n\ge1} \Lambda_{mn}^{2s} |v_{mn}|^2.$$

Given a source f, an initial datum u_0, and a final time $T > 0$, the model problem is

$$\begin{cases} u_t(x,y,t) = -\varphi(B)u(x,y,t) + f(x,y,t), & (x,y) \in \Omega, \quad 0 < t \le T, \\ u(x,y,t) = 0, & (x,y) \in \partial\Omega, \\ u(x,y,0) = u_0(x,y). \end{cases} \tag{2.2}$$

The homogeneous Dirichlet condition in (2.2) is imposed for every $(x,y) \in \partial\Omega$ and every $t \in (0,T]$.

3. Compact generator and functional-calculus transfer

Let $h_z = L_z/M_z$, $z = x, y$, and use the interior grid points $z_j = jh_z$, $j = 1, \ldots, M_z - 1$. We assume a quasi-uniform family of rectangular grids: there exists a constant $\gamma \geq 1$, independent of the mesh size, such that

$$\gamma^{-1} \leq \frac{h_x}{h_y} \leq \gamma.$$

Throughout this section, $h = \max\{h_x, h_y\}$. Hence, h_x, h_y, and h are comparable. Generic constants may depend on $L_x, L_y, \gamma, \mu^\pm, \rho$, and on fixed exponents appearing in the estimates, but not on the mesh sizes or modal indices.

Set

$$T_{z,h} = h_z^{-2}\,\mathrm{tridiag}(-1, 2, -1), \qquad P_{z,h} = I - \frac{h_z^2}{12} T_{z,h},$$

and define the compact one-dimensional positive Laplacian

$$A_{z,h}^{(4)} = P_{z,h}^{-1} T_{z,h}.$$

The discrete sine basis diagonalizes both $T_{z,h}$ and $A_{z,h}^{(4)}$. If

$$\theta_{m,z} = 4h_z^{-2} \sin^2 \frac{m\pi}{2M_z},$$

then

$$a_{m,z}^{(4)} = \frac{\theta_{m,z}}{1 - h_z^2 \theta_{m,z}/12} = \frac{4h_z^{-2} \sin^2(m\pi/(2M_z))}{1 - \frac{1}{3} \sin^2(m\pi/(2M_z))}. \tag{3.1}$$

Here the factor $1/3$ follows directly from $h_z^2 \theta_{m,z}/12 = (4/12) \sin^2(m\pi/(2M_z)) = \frac{1}{3} \sin^2(m\pi/(2M_z))$.

Lemma 1 (One-dimensional compact eigenvalue estimates; see [13, 14])**.** *There exist mesh-independent constants $c, C > 0$ such that*

$$c\kappa_{m,z}^2 \leq a_{m,z}^{(4)} \leq C\kappa_{m,z}^2$$

and

$$\left|a_{m,z}^{(4)} - \kappa_{m,z}^2\right| \leq Ch_z^4 \kappa_{m,z}^6, \qquad 1 \leq m \leq M_z - 1.$$

Proof. The spectral equivalence follows from $\sin r \asymp r$ on $0 \leq r \leq \pi/2$, and from

$$1 - h_z^2 \theta_{m,z}/12 = 1 - \frac{1}{3} \sin^2(m\pi/(2M_z)) \in [2/3, 1].$$

For the perturbation estimate, set $x = m\pi/M_z = \kappa_{m,z} h_z$ and

$$b(x) = \frac{4 \sin^2(x/2)}{1 - \frac{1}{3} \sin^2(x/2)}.$$

Then $a_{m,z}^{(4)} = h_z^{-2} b(x)$. As $x \to 0$,

$$4\sin^2(x/2) = x^2 - \frac{x^4}{12} + \frac{x^6}{360} + O(x^8),$$
$$\left(1 - \frac{1}{3}\sin^2(x/2)\right)^{-1} = 1 + \frac{x^2}{12} - \frac{x^6}{2880} + O(x^8).$$

Multiplying these expansions gives

$$b(x) = x^2 + \left(\frac{1}{360} - \frac{1}{144}\right)x^6 + O(x^8) = x^2 - \frac{x^6}{240} + O(x^8).$$

Consequently, $(b(x) - x^2)/x^6 \to -1/240$ as $x \to 0$. By the denominator bound above, this quotient extends continuously to $[0, \pi]$ and is bounded there. Hence,

$$\left|a_{m,z}^{(4)} - \kappa_{m,z}^2\right| = h_z^{-2}|b(x) - x^2| \le C h_z^{-2} x^6 = C h_z^4 \kappa_{m,z}^6.$$

□

The two-dimensional compact generator is the Kronecker sum

$$A_{\Delta,h}^{(4)} = I_y \otimes A_{x,h}^{(4)} + A_{y,h}^{(4)} \otimes I_x,$$

where I_x and I_y are identity matrices of the appropriate one-dimensional sizes. For grid vectors $V, W \in \mathbb{R}^{(M_x-1)(M_y-1)}$, ordered consistently with the tensor-product grid, we use

$$(V, W)_h = h_x h_y \sum_{i=1}^{M_x-1} \sum_{j=1}^{M_y-1} V_{ij} W_{ij}, \qquad \|V\|_h = (V, V)_h^{1/2}.$$

Let $\mathcal{S}_h = S_y \otimes S_x$ denote the tensor-product DST-I matrix, normalized to be orthonormal in the Euclidean inner product. If $\widehat{V} = \mathcal{S}_h^T V$, then the discrete Parseval identity used below is

$$\|V\|_h^2 = h_x h_y \sum_{m=1}^{M_x-1} \sum_{n=1}^{M_y-1} |\widehat{V}_{mn}|^2.$$

With this convention,

$$A_{\Delta,h}^{(4)} = \mathcal{S}_h \ \mathrm{diag}\{\mathcal{A}_{mn,h}^{(4)}\}\, \mathcal{S}_h^T, \qquad \mathcal{A}_{mn,h}^{(4)} = a_{m,x}^{(4)} + a_{n,y}^{(4)}.$$

Matrix functional calculus provides a standard framework for applying functions to discrete elliptic generators in the approximation of fractional elliptic operators [10, 11, 37–39].

Lemma 2 (Two-dimensional compact generator estimates [13, 14]). *For all resolved modes,*

$$c\Lambda_{mn} \le \mathcal{A}_{mn,h}^{(4)} \le C\Lambda_{mn}$$

and

$$|\mathcal{A}_{mn,h}^{(4)} - \Lambda_{mn}| \le C(h_x^4 + h_y^4)\Lambda_{mn}^3.$$

Proof. The first assertion follows by adding the one-dimensional spectral equivalences. For the perturbation,

$$|\mathcal{A}^{(4)}_{mn,h} - \Lambda_{mn}| \le C\left(h_x^4\kappa_{m,x}^6 + h_y^4\kappa_{n,y}^6\right).$$

The exponent 3 comes from expressing the sixth-power wavenumber factors in Lemma 1 on the Laplacian eigenvalue scale. Indeed, using $\Lambda_{mn} = \kappa_{m,x}^2 + \kappa_{n,y}^2$,

$$\begin{aligned} h_x^4\kappa_{m,x}^6 + h_y^4\kappa_{n,y}^6 &\le (h_x^4 + h_y^4)\left(\kappa_{m,x}^6 + \kappa_{n,y}^6\right) \\ &\le (h_x^4 + h_y^4)\left(\kappa_{m,x}^2 + \kappa_{n,y}^2\right)^3 \\ &= (h_x^4 + h_y^4)\Lambda_{mn}^3. \end{aligned}$$

□

Lemma 3 (Full-spectral transfer through φ)**.** *Under Assumption 1,*

$$\left|\varphi(\mathcal{A}^{(4)}_{mn,h}) - \varphi(\Lambda_{mn})\right| \le C(h_x^4 + h_y^4)\Lambda_{mn}^{\mu^+/2+2}.$$

Proof. For a fixed $\mu \in [\mu^-, \mu^+]$, set $\alpha = \mu/2 \in [\mu^-/2, \mu^+/2] \subset (0, 1]$ and define

$$I_{mn,h} := [\min\{\mathcal{A}^{(4)}_{mn,h}, \Lambda_{mn}\}, \max\{\mathcal{A}^{(4)}_{mn,h}, \Lambda_{mn}\}].$$

By Lemma 2, $I_{mn,h} \subset [c_0\Lambda_{mn}, C_0\Lambda_{mn}] \subset (0, \infty)$ for mesh- and mode-independent constants $c_0, C_0 > 0$. If the two endpoints coincide, the following estimate is immediate. Otherwise, the mean value theorem applied to s^α on $I_{mn,h}$ gives, for some $\xi_{mn,h} \in \mathrm{int}(I_{mn,h})$,

$$\begin{aligned} \left|(\mathcal{A}^{(4)}_{mn,h})^\alpha - \Lambda_{mn}^\alpha\right| &= \alpha\xi_{mn,h}^{\alpha-1}|\mathcal{A}^{(4)}_{mn,h} - \Lambda_{mn}| \\ &\le C\Lambda_{mn}^{\alpha-1}|\mathcal{A}^{(4)}_{mn,h} - \Lambda_{mn}| \\ &\le C(h_x^4 + h_y^4)\Lambda_{mn}^{\alpha+2}. \end{aligned}$$

Since $\Lambda_{mn} \ge \Lambda_{11} > 0$, integrating the last bound against $\rho(\mu)\,\mathrm{d}\mu$ and using $\alpha \le \mu^+/2$ gives the result. □

Let R_h be a pointwise grid restriction and let Π_h be the continuous sine projection onto the modes $1 \le m \le M_x - 1$, $1 \le n \le M_y - 1$ resolved by the grid. For a sampled function w, write $\widehat{(R_h w)} = \mathcal{S}_h^T R_h w$. The following sampling statement is standard for sine-series traces; the square-shell count in Appendix A shows that the unresolved two-dimensional lattice sum is comparable to $\sum_{j\ge1} j^{1-2r}$, which converges exactly for $r > 1$ and diverges logarithmically at $r = 1$.

Lemma 4 (Sine sampling and high-frequency aliasing; see [40, 41])**.** *If $r > 1$ and $w \in D(B^{r/2})$, then*

$$\|R_h(I - \Pi_h)w\|_h \le Ch^r \left\|B^{r/2}w\right\|_{L^2}.$$

If $\sigma > 1$ and $w \in D(B^{\sigma/2})$, then

$$\|R_h w\|_h \le C\left\|B^{\sigma/2}w\right\|_{L^2}.$$

More generally, for any $\beta \ge 0$, $\sigma > 1$, and $w \in D(B^{(\beta+\sigma)/2})$,

$$\left(h_x h_y \sum_{p=1}^{M_x-1}\sum_{q=1}^{M_y-1} \Lambda_{pq}^\beta|\widehat{(R_h w)}_{pq}|^2\right)^{1/2} \le C\left\|B^{(\beta+\sigma)/2}w\right\|_{L^2}.$$

Theorem 1 (Fourth-order compact functional-calculus consistency)**.** *Under Assumption 1 and the quasi-uniform grid condition above, if $v \in D(B^{\mu^+/2+2})$, then*

$$\left\| R_h\varphi(B)v - \varphi(A^{(4)}_{\Delta,h})R_h v \right\|_h \le Ch^4 \left\| B^{\mu^+/2+2} v \right\|_{L^2}.$$

Proof. For $\Pi_h v$, Parseval's identity and Lemma 3 yield, with the sum over resolved modes and $h_x^4 + h_y^4 \le Ch^4$,

$$\begin{aligned}\left\| R_h\varphi(B)\Pi_h v - \varphi(A^{(4)}_{\Delta,h})R_h\Pi_h v \right\|_h^2 &\le Ch^8 \sum_{m,n} \Lambda_{mn}^{2(\mu^+/2+2)} |v_{mn}|^2 \\ &\le Ch^8 \left\| B^{\mu^+/2+2} v \right\|_{L^2}^2.\end{aligned}$$

For the continuous high-frequency tail, Lemma 4 with $r = 4$ gives

$$\begin{aligned}\| R_h\varphi(B)(I-\Pi_h)v \|_h &\le Ch^4 \left\| B^2\varphi(B)(I-\Pi_h)v \right\|_{L^2} \\ &\le Ch^4 \left\| B^{\mu^+/2+2} v \right\|_{L^2}\end{aligned}$$

because $\varphi(s) \le Cs^{\mu^+/2}$ for $s \ge \Lambda_{11}$. For the discrete high-frequency tail, Lemma 2 and the quasi-uniformity of the grid imply

$$\begin{aligned} a^{(4)}_{m,z} &\overset{(3.1)}{\le} \frac{4h_z^{-2}}{2/3} = 6h_z^{-2}, \qquad z = x, y, \\ \max_{m,n} \mathcal{A}^{(4)}_{mn,h} &= \max_{m,n}(a^{(4)}_{m,x} + a^{(4)}_{n,y}) \\ &\le 6(h_x^{-2} + h_y^{-2}) \le 6(1+\gamma^2)h^{-2} = Ch^{-2}, \end{aligned}$$

and hence,

$$\left\| \varphi(A^{(4)}_{\Delta,h})R_h(I-\Pi_h)v \right\|_h \le Ch^{-\mu^+} \| R_h(I-\Pi_h)v \|_h.$$

Applying Lemma 4 with $r = \mu^+ + 4$ yields

$$\begin{aligned}\left\| \varphi(A^{(4)}_{\Delta,h})R_h(I-\Pi_h)v \right\|_h &\le Ch^{-\mu^+} h^{\mu^+ + 4} \left\| B^{(\mu^+ + 4)/2} v \right\|_{L^2} \\ &= Ch^4 \left\| B^{\mu^+/2+2} v \right\|_{L^2}.\end{aligned}$$

Combining the resolved part and the two tail estimates gives the stated estimate. □

Set $\alpha_+ := \mu^+/2$. The assumption $v \in D(B^{\mu^+/2+2})$ is sufficient for attaining the $O(h^4)$ spatial rate; under lower regularity, Corollary 1 gives the corresponding rate $q(s) = \min\{4, 2(s - \alpha_+)\}$.

Corollary 1 (Regularity-rate tradeoff)**.** *Under Assumption 1 and the quasi-uniform grid condition, assume that $v \in D(B^s)$ with $s > \alpha_+ + 1/2$. Then*

$$\left\| R_h\varphi(B)v - \varphi(A^{(4)}_{\Delta,h})R_h v \right\|_h \le Ch^{q(s)} \| B^s v \|_{L^2}, \qquad q(s) = \min\{4,\ 2(s-\alpha_+)\}.$$

In particular, the fourth-order estimate in Theorem 1 is recovered when $s \ge \alpha_+ + 2$.

Proof. If $s \ge \alpha_+ + 2$, the assertion follows directly from Theorem 1. It remains to consider $\alpha_+ + 1/2 < s < \alpha_+ + 2$, for which $q(s) = 2(s - \alpha_+) > 1$.

For the resolved modes, Lemma 3 gives

$$|\varphi(\mathcal{A}^{(4)}_{mn,h}) - \varphi(\Lambda_{mn})| \le Ch^4 \Lambda_{mn}^{\alpha_+ + 2}.$$

Set $\delta = \alpha_+ + 2 - s > 0$. Since the resolved eigenvalues satisfy $\Lambda_{mn} \le Ch^{-2}$,

$$\begin{aligned} h^4 \Lambda_{mn}^{\alpha_+ + 2} &= h^{2(s-\alpha_+)} \Lambda_{mn}^{s} (h^2 \Lambda_{mn})^{\delta} \\ &\le Ch^{2(s-\alpha_+)} \Lambda_{mn}^{s}. \end{aligned}$$

Thus, the factor 2 in the lower-regularity rate comes from the $O(h^{-2})$ spectral scaling of the resolved eigenvalues. Parseval's identity therefore bounds the resolved-mode contribution by $Ch^{q(s)} \|B^s v\|_{L^2}$.

For the continuous high-frequency tail, apply Lemma 4 with $r = q(s) > 1$ to $w = \varphi(B)(I - \Pi_h)v$, which has no resolved modes. Since $\varphi(\lambda) \le C\lambda^{\alpha_+}$,

$$\|R_h \varphi(B)(I - \Pi_h)v\|_h \le Ch^{q(s)} \left\| B^{q(s)/2} \varphi(B) v \right\|_{L^2} \le Ch^{q(s)} \|B^s v\|_{L^2}.$$

For the discrete high-frequency tail, Lemma 2, the DST diagonalization, and $\max_{m,n} \mathcal{A}^{(4)}_{mn,h} \le Ch^{-2}$ show that the induced discrete L^2-operator norm satisfies

$$\sup_{W \ne 0} \frac{\left\| \varphi(A^{(4)}_{\Delta,h}) W \right\|_h}{\|W\|_h} = \max_{m,n} \varphi(\mathcal{A}^{(4)}_{mn,h}) \le Ch^{-2\alpha_+}.$$

Taking $W = R_h(I - \Pi_h)v$ and using Lemma 4 with $r = 2s > 1$,

$$\left\| \varphi(A^{(4)}_{\Delta,h}) R_h (I - \Pi_h) v \right\|_h \le Ch^{-2\alpha_+} \|R_h (I - \Pi_h) v\|_h \le Ch^{2s - 2\alpha_+} \|B^s v\|_{L^2}.$$

Since $2s - 2\alpha_+ = q(s)$, the three bounds give the result. □

4. Unsplit modal Crank–Nicolson scheme

Define $\Phi_h = \varphi(A^{(4)}_{\Delta,h})$ and $L_h = -\Phi_h$. In modal form,

$$\Phi_h = \mathcal{S}_h \,\mathrm{diag}\{\psi_{mn,h}\}\, \mathcal{S}_h^T, \qquad \psi_{mn,h} = \varphi(\mathcal{A}^{(4)}_{mn,h}) > 0.$$

The semi-discrete generator is therefore self-adjoint and nonpositive with respect to the discrete inner product $(\cdot, \cdot)_h$. Let $N_t \tau = T$ and use the time grid

$$t_n = n\tau, \qquad n = 0, \ldots, N_t, \qquad t_{n+1/2} = t_n + \frac{\tau}{2}.$$

With $U^0 = R_h u_0$ and $F^{n+1/2} = R_h f(t_{n+1/2})$, the fully discrete method is

$$\frac{U^{n+1} - U^n}{\tau} = L_h \frac{U^{n+1} + U^n}{2} + F^{n+1/2}. \tag{4.1}$$

Equivalently, (4.1) can be written as

$$\left(I - \frac{\tau}{2} L_h\right) U^{n+1} = \left(I + \frac{\tau}{2} L_h\right) U^n + \tau F^{n+1/2}. \tag{4.2}$$

Since $L_h = -\Phi_h$, this is also

$$\left(I + \frac{\tau}{2}\Phi_h\right) U^{n+1} = \left(I - \frac{\tau}{2}\Phi_h\right) U^n + \tau F^{n+1/2}.$$

Let $\widehat{U^n} = \mathcal{S}_h^T U^n$ and $\widehat{F^{n+1/2}} = \mathcal{S}_h^T F^{n+1/2}$. Each mode is updated by the scalar formula

$$\widehat{U}_{mn}^{n+1} = \frac{1 - \frac{\tau}{2}\psi_{mn,h}}{1 + \frac{\tau}{2}\psi_{mn,h}} \widehat{U}_{mn}^{n} + \frac{\tau}{1 + \frac{\tau}{2}\psi_{mn,h}} \widehat{F}_{mn}^{n+1/2}. \tag{4.3}$$

The homogeneous amplification factor $G_{mn} = (1 - \frac{\tau}{2}\psi_{mn,h})/(1 + \frac{\tau}{2}\psi_{mn,h})$ satisfies $|G_{mn}| \leq 1$, because $\tau > 0$ and $\psi_{mn,h} > 0$ imply $\left|1 - \frac{\tau}{2}\psi_{mn,h}\right| \leq 1 + \frac{\tau}{2}\psi_{mn,h}$. The update is unsplit: it applies the scalar function to the full two-dimensional eigenvalue $\mathcal{A}_{mn,h}^{(4)}$, rather than factorizing the step into coordinate directions. This distinguishes (4.3) from classical ADI factorizations and related distributed-order Riesz schemes based on directional or spectral discretizations [28, 29, 42, 43].

4.1. Positive quadrature of the order integral

When the order integral is evaluated by quadrature, we use a positive rule:

$$\varphi_J(s) = \sum_{q=1}^{J} \omega_q \rho(\mu_q) s^{\mu_q/2}, \qquad \mu_q \in [\mu^-, \mu^+], \quad \omega_q > 0.$$

The number of order-quadrature nodes is denoted by J in the analysis and the numerical tables report the same quantity as J_μ. Quadrature reduction of the distributed-order integral is common in finite-difference, spectral, and Laplace-transform-based methods [9, 44, 45].

The continuous assumption $\rho \in L^1$ is sufficient to define φ, but nodal quadrature requires a representative that can be evaluated at the quadrature nodes. We therefore impose the following separate assumption only for quadrature-based computations and estimates.

Assumption 2 (Quadrature-compatible order rule)**.** *The quadrature nodes satisfy $\mu_q \in [\mu^-, \mu^+]$, the weights satisfy $\omega_q > 0$, the selected representative of ρ is nonnegative at the nodes, and the nodal mass obeys*

$$\sum_{q=1}^{J} \omega_q \rho(\mu_q) > 0.$$

Assumption 2 makes no convergence claim for nodal quadrature under only L^1 regularity of ρ. For smooth densities, positive Gauss–Legendre rules are a standard choice, and in the analysis below, the resulting order-quadrature contribution is kept as the separate budget E_μ.

Under the nodal density conditions above, positive weights give a simple grid-independent sufficient condition for modal positivity. For a signed rule, unconditional CN stability on a fixed grid holds if and only if $\varphi_J(\mathcal{A}_{mn,h}^{(4)}) \geq 0$ for every resolved mode. If this quantity is negative for any mode, the corresponding amplification factor in (4.3) has a modulus greater than one and its denominator vanishes at $\tau = -2/\varphi_J(\mathcal{A}_{mn,h}^{(4)}) > 0$.

The quadrature operators are $\Phi_{h,J} = \varphi_J(A_{\Delta,h}^{(4)})$ and $L_{h,J} = -\Phi_{h,J}$. Under Assumption 2, $\varphi_J(s) > 0$ for $s > 0$, so quadrature preserves dissipativity. The quadrature CN solution obtained by replacing L_h with $L_{h,J}$ in (4.1) is denoted by U_J^n.

For a grid vector V, write $\widehat{V} = \mathcal{S}_h^T V$ and define

$$E_{\mu,h}(V) = (h_x h_y)^{1/2} \left(\sum_{m=1}^{M_x-1} \sum_{n=1}^{M_y-1} \left| \varphi_J(\mathcal{A}^{(4)}_{mn,h}) - \varphi(\mathcal{A}^{(4)}_{mn,h}) \right|^2 |\widehat{V}_{mn}|^2 \right)^{1/2}.$$

By the discrete Parseval identity, the modal expression above is exactly the standard discrete L^2 norm $E_{\mu,h}(V) = \left\| (\Phi_{h,J} - \Phi_h) V \right\|_h$. For an exact solution sampled at the time levels of the CN scheme, set

$$E_\mu = \max_{0 \le n \le N_t - 1} E_{\mu,h}\left(\frac{R_h u(t_{n+1}) + R_h u(t_n)}{2} \right).$$

Thus E_μ is a separate order-quadrature budget for the particular solution and quadrature rule, not a spatial consistency term. For endpoint-concentrated densities, this order-quadrature contribution may dominate the $O(h^4)$ spatial term at moderate J_μ; the operator-action discrepancies in Table 7 illustrate this possibility. The quadrature estimates below are conditional on this finite budget E_μ.

4.2. Algorithm and complexity

The implementation uses only two-dimensional DSTs and modal multiplication. The transforms DST2 and IDST2 use the same orthonormal DST-I normalization as $\mathcal{S}_h$. Let $\psi^*_{mn,h}$ denote the working modal symbol:

$$\psi^*_{mn,h} = \psi_{mn,h} \quad \text{for exact-symbol runs}, \qquad \psi^*_{mn,h} = \varphi_J(\mathcal{A}^{(4)}_{mn,h}) \quad \text{for quadrature runs}.$$

1) Precompute $a^{(4)}_{m,x}$, $a^{(4)}_{n,y}$, $\mathcal{A}^{(4)}_{mn,h} = a^{(4)}_{m,x} + a^{(4)}_{n,y}$, and $\psi^*_{mn,h}$.
2) Precompute

$$G^*_{mn} = \frac{1 - \frac{\tau}{2}\psi^*_{mn,h}}{1 + \frac{\tau}{2}\psi^*_{mn,h}}, \qquad D^*_{mn} = \frac{\tau}{1 + \frac{\tau}{2}\psi^*_{mn,h}}.$$

3) At each step, compute $\widehat{U^n} = \mathrm{DST2}(U^n)$ and $\widehat{F^{n+1/2}} = \mathrm{DST2}(F^{n+1/2})$, update

$$\widehat{U}^{n+1}_{mn} = G^*_{mn} \widehat{U}^n_{mn} + D^*_{mn} \widehat{F}^{n+1/2}_{mn},$$

and transform back with IDST2.

For $N_{\mathrm{dof}} = (M_x - 1)(M_y - 1)$, exact-symbol precomputation requires $O(N_{\mathrm{dof}})$ scalar evaluations when φ is available analytically, while quadrature-based precomputation with J nodes costs $O(JN_{\mathrm{dof}})$. Each time step costs $O(N_{\mathrm{dof}} \log N_{\mathrm{dof}})$ and storage is $O(N_{\mathrm{dof}})$. No dense two-dimensional matrix function is formed.

Contour-integral, shifted-resolvent, and rational Krylov methods [11, 37, 39] support more general matrices and geometries, with matrix-function actions evaluated through multiple shifted linear solves or Krylov iterations. Distributed-order Riesz ADI/proper orthogonal decomposition (POD) schemes [28, 29] use directional or reduced-order solvers for their Riesz spatial operators. On separable Dirichlet grids, the fixed-order compact matrix-transfer/DST method [25] has a transform-dominated $O(N_{\mathrm{dof}} \log N_{\mathrm{dof}})$ spatial cost. The present distributed-order formulation retains this online complexity: the J-node order quadrature is confined to a one-time $O(JN_{\mathrm{dof}})$ symbol construction, after which each CN step costs $O(N_{\mathrm{dof}} \log N_{\mathrm{dof}})$, uses $O(N_{\mathrm{dof}})$ storage, and is independent of J. Thus, in the separable setting considered here, its computational advantage is a direct DST-based update with neither repeated shifted solves nor J-dependent work at each time step.

5. Stability and convergence

Lemma 5 (Positivity and dissipativity; see [10, 36]). *Under Assumption 1, Φ_h is symmetric positive definite and $L_h = -\Phi_h$ is dissipative in the discrete inner product:*

$$(\Phi_h V, V)_h > 0 \quad (V \neq 0), \qquad (L_h V, V)_h \leq 0.$$

The same statements hold for $\Phi_{h,J}$ and $L_{h,J}$ under Assumption 2.

Proof. The eigenvalues of $A^{(4)}_{\Delta,h}$ are $\mathcal{A}^{(4)}_{mn,h} > 0$, and $\varphi(s) > 0$ for $s > 0$. Hence, the modal eigenvalues $\psi_{mn,h}$ of Φ_h are positive. For the quadrature operator, the modal eigenvalues are $\varphi_J(\mathcal{A}^{(4)}_{mn,h})$, which are positive under Assumption 2. Writing $\widehat{V} = \mathcal{S}_h^T V$, the orthonormal DST normalization and the definition of $(\cdot,\cdot)_h$ give

$$(\Phi_h V, V)_h = h_x h_y \widehat{V}^T \operatorname{diag}\{\psi_{mn,h}\}\widehat{V} = h_x h_y \sum_{m=1}^{M_x-1}\sum_{n=1}^{M_y-1} \psi_{mn,h}|\widehat{V}_{mn}|^2,$$

$$(L_h V, V)_h = -(\Phi_h V, V)_h = -h_x h_y \sum_{m=1}^{M_x-1}\sum_{n=1}^{M_y-1} \psi_{mn,h}|\widehat{V}_{mn}|^2.$$

For $V \neq 0$, orthogonality gives $\widehat{V} \neq 0$. Since every $\psi_{mn,h} > 0$, the first quantity is strictly positive and the second is nonpositive. Replacing $\psi_{mn,h}$ by $\varphi_J(\mathcal{A}^{(4)}_{mn,h}) > 0$ gives the same identities for $\Phi_{h,J}$ and $L_{h,J}$ under Assumption 2. □

Theorem 2 (Unconditional discrete L^2 stability). *Under Assumption 1, for every $\tau > 0$, the linear system in* (4.2) *is uniquely solvable. For the homogeneous problem $F^{n+1/2} = 0$, scheme* (4.1) *satisfies*

$$\left\|U^{n+1}\right\|_h \leq \|U^n\|_h, \qquad \tau > 0.$$

For the nonhomogeneous problem,

$$\|U^n\|_h \leq \left\|U^0\right\|_h + \tau \sum_{k=0}^{n-1} \left\|F^{k+1/2}\right\|_h.$$

Under Assumption 2, the same solvability and estimates hold for the quadrature scheme obtained by replacing L_h with $L_{h,J}$.

Proof. Since Φ_h is symmetric positive definite, $I - \tau L_h/2 = I + \tau\Phi_h/2$ is symmetric positive definite and hence invertible. The exact-symbol homogeneous modal amplification factor is

$$G_{mn} = \frac{1 - \frac{\tau}{2}\psi_{mn,h}}{1 + \frac{\tau}{2}\psi_{mn,h}},$$

and $|G_{mn}| \leq 1$ for every $\tau > 0$. For the nonhomogeneous recurrence, the forcing coefficient satisfies

$$0 < \frac{\tau}{1 + \frac{\tau}{2}\psi_{mn,h}} \leq \tau.$$

On a fixed grid, the largest modal forcing coefficient is $\tau/(1 + \frac{\tau}{2}\psi_{\min,h}) < \tau$, where $\psi_{\min,h} := \min_{m,n} \psi_{mn,h} > 0$. Its ratio to τ tends to one as $\tau \to 0^+$, so the factor τ is asymptotically sharp.

Thus (4.3), Parseval's identity, and summation in time give the stated bound. For the quadrature scheme, replace $\psi_{mn,h}$ by $\varphi_J(\mathcal{A}^{(4)}_{mn,h}) > 0$ and repeat the same modal argument. This is the standard CN contraction argument [14, 42]. □

Lemma 6 (Discrete operator bound; cf. [10, 40])**.** *Under Assumption 1, let $\sigma > 1$. If $v \in D(B^{(\mu^+ +\sigma)/2})$, then*

$$\|\Phi_h R_h v\|_h = \|L_h R_h v\|_h \leq C \left\|B^{(\mu^+ +\sigma)/2} v\right\|_{L^2}.$$

Proof. On resolved modes, $\psi_{mn,h} \leq C\Lambda_{mn}^{\mu^+/2}$ by Lemma 2 and $\varphi(s) \leq Cs^{\mu^+/2}$. Therefore, with $\widehat{(R_h v)} = \mathcal{S}_h^T R_h v$,

$$\begin{aligned}\|\Phi_h R_h v\|_h^2 &= h_x h_y \sum_{p,q} \psi_{pq,h}^2 |\widehat{(R_h v)}_{pq}|^2 \\ &\leq C h_x h_y \sum_{p,q} \Lambda_{pq}^{\mu^+} |\widehat{(R_h v)}_{pq}|^2.\end{aligned}$$

The weighted trace bound in Lemma 4, with $\beta = \mu^+$, gives

$$h_x h_y \sum_{p,q} \Lambda_{pq}^{\mu^+} |\widehat{(R_h v)}_{pq}|^2 \leq C \left\|B^{(\mu^+ +\sigma)/2} v\right\|_{L^2}^2.$$

Since $L_h = -\Phi_h$, the same bound holds for $L_h R_h v$. This proves the result. The condition $\sigma > 1$ supplies the additional spatial spectral decay required to make the two-dimensional pointwise-sampling alias factor $\sup_{p,q} \sum_{(m,n)\in C_{pq}} \Lambda_{mn}^{-\sigma}$ finite; the shell/integral proof is given in Appendix A. □

Let $u_h^n = R_h u(t_n)$ and define

$$\delta_t u_h^{n+1/2} = \frac{u_h^{n+1} - u_h^n}{\tau}, \qquad \overline{u}_h^{n+1/2} = \frac{u_h^{n+1} + u_h^n}{2}.$$

The exact-symbol local residual is

$$\mathcal{T}^{n+1/2} = \delta_t u_h^{n+1/2} - L_h \overline{u}_h^{n+1/2} - R_h f(t_{n+1/2}).$$

For the quadrature operator, we use

$$\mathcal{T}_J^{n+1/2} = \delta_t u_h^{n+1/2} - L_{h,J} \overline{u}_h^{n+1/2} - R_h f(t_{n+1/2}).$$

Because no directional product factorization is used, no mixed splitting residual appears.

Theorem 3 (Local truncation error)**.** *Under Assumption 1 and the quasi-uniform grid condition, let $\sigma > 1$. Suppose*

$$\begin{aligned} u &\in C([0,T]; D(B^{\mu^+/2+2})), \\ u_{tt} &\in L^\infty(0,T; D(B^{(\mu^+ +\sigma)/2})), \\ u_{ttt} &\in L^\infty(0,T; D(B^{\sigma/2})). \end{aligned}$$

Then, for $0 \leq n \leq N_t - 1$,

$$\left\|\mathcal{T}^{n+1/2}\right\|_h \leq C(\tau^2 + h^4).$$

With quadrature under Assumption 2, the bound becomes

$$\left\|\mathcal{T}_J^{n+1/2}\right\|_h \le C(\tau^2 + h^4 + E_\mu),$$

where E_μ is the order-quadrature budget defined in Section 4. The constant C is independent of h, τ, and n.

Proof. Using the continuous equation $u_t(t_{n+1/2}) = Lu(t_{n+1/2}) + f(t_{n+1/2})$, decompose the residual as

$$\begin{aligned}\mathcal{T}^{n+1/2} = &\left(\delta_t u_h^{n+1/2} - R_h u_t(t_{n+1/2})\right)\\ &+ (R_h L u(t_{n+1/2}) - L_h R_h u(t_{n+1/2}))\\ &+ L_h\left(R_h u(t_{n+1/2}) - \overline{u}_h^{n+1/2}\right).\end{aligned}$$

The centered time derivative satisfies

$$\left\|\delta_t u_h^{n+1/2} - R_h u_t(t_{n+1/2})\right\|_h \le C\tau^2 \|u_{ttt}\|_{L^\infty(t_n,t_{n+1};D(B^{\sigma/2}))}$$

by Taylor expansion and Lemma 4. By the first regularity assumption,

$$K_u := \max_{0\le t\le T}\left\|B^{\mu^+/2+2}u(t)\right\|_{L^2} < \infty.$$

Applying Theorem 1 with $v = u(t_{n+1/2})$ gives

$$\begin{aligned}&\left\|R_h L u(t_{n+1/2}) - L_h R_h u(t_{n+1/2})\right\|_h\\ &= \left\|R_h \varphi(B) u(t_{n+1/2}) - \varphi(A_{\Delta,h}^{(4)}) R_h u(t_{n+1/2})\right\|_h\\ &\le Ch^4\left\|B^{\mu^+/2+2}u(t_{n+1/2})\right\|_{L^2} \le Ch^4 K_u,\end{aligned}$$

uniformly for $0 \le n \le N_t - 1$. Writing $t_c = t_{n+1/2}$, the two centered Taylor formulas with integral remainders are

$$\begin{aligned}u\left(t_c \pm \frac{\tau}{2}\right) = &\ u(t_c) \pm \frac{\tau}{2}u_t(t_c)\\ &+ \frac{\tau^2}{4}\int_0^1 (1-\xi)u_{tt}\left(t_c \pm \frac{\xi\tau}{2}\right)\,\mathrm{d}\xi.\end{aligned}$$

The first-derivative terms have opposite signs and cancel when the two identities are averaged. By the linearity of R_h, the change of variables $\theta = \pm\xi/2$ then gives the exact midpoint remainder

$$\overline{u}_h^{n+1/2} - R_h u(t_{n+1/2}) = \frac{\tau^2}{2}\int_{-1/2}^{1/2}\left(\frac{1}{2} - |\theta|\right) R_h u_{tt}(t_{n+1/2} + \theta\tau)\,\mathrm{d}\theta.$$

Consequently, Lemma 6 and the stated u_{tt} regularity give

$$\left\|L_h\left(R_h u(t_{n+1/2}) - \overline{u}_h^{n+1/2}\right)\right\|_h \le C\tau^2 \|u_{tt}\|_{L^\infty(t_n,t_{n+1};D(B^{(\mu^+ + \sigma)/2}))}.$$

For the quadrature residual,

$$\mathcal{T}_J^{n+1/2} = \mathcal{T}^{n+1/2} + (\Phi_{h,J} - \Phi_h)\overline{u}_h^{n+1/2},$$

and the last term is bounded by $E_{\mu,h}(\overline{u}_h^{n+1/2}) \le E_\mu$ by the definition in Section 4. The temporal-discretization estimates follow from the standard centered-difference and midpoint Taylor expansions [14, 42]. □

Theorem 4 (Fully discrete convergence)**.** *Assume the hypotheses of Theorem 3 and set $U^0 = R_h u_0$. Then*

$$\|R_h u(t_n) - U^n\|_h \leq C(\tau^2 + h^4), \qquad 0 \leq t_n \leq T.$$

With quadrature under Assumption 2, if $U_J^0 = R_h u_0$, then

$$\left\|R_h u(t_n) - U_J^n\right\|_h \leq C(\tau^2 + h^4 + E_\mu), \qquad 0 \leq t_n \leq T.$$

In both estimates, $C = C_T$ is independent of h, τ, and n for each fixed final time T.

Proof. Let $e^n = R_h u(t_n) - U^n$. Subtracting the numerical scheme from the residual equation gives

$$\left(I - \frac{\tau}{2} L_h\right) e^{n+1} = \left(I + \frac{\tau}{2} L_h\right) e^n + \tau \mathcal{T}^{n+1/2}.$$

The nonhomogeneous stability estimate in Theorem 2 gives

$$\|e^n\|_h \leq \left\|e^0\right\|_h + \tau \sum_{k=0}^{n-1} \left\|\mathcal{T}^{k+1/2}\right\|_h.$$

Since $e^0 = 0$, Theorem 3 yields

$$\|e^n\|_h \leq C(\tau^2 + h^4), \qquad 0 \leq t_n \leq T,$$

with T absorbed into the constant. For the quadrature statement, use $e_J^n = R_h u(t_n) - U_J^n$, the residual $\mathcal{T}_J^{n+1/2}$, and the quadrature version of Theorem 2. □

Remark 1. *The regularity assumptions in Theorem 3 are sufficient for the convergence proof because they provide the bounds required for the three components of the local residual. The condition $u \in C([0, T]; D(B^{\mu^+/2+2}))$ makes the required graph-domain bound available at every time and is used for the fourth-order spatial transfer in Theorem 1. Replacing Theorem 1 by Corollary 1 gives the corresponding local and fully discrete estimates with h^4 replaced by $h^{q(s)}$, provided this first regularity condition is replaced by $u \in C([0, T]; D(B^s))$, while the stated assumptions on u_{tt} and u_{ttt} are retained. These assumptions on u_{tt} and u_{ttt} enter only through the midpoint average and the centered time difference, respectively. The restriction $\sigma > 1$ is the two-dimensional pointwise-sampling threshold in Lemma 4, arising from convergence of the alias lattice sum in Appendix A. Under these assumptions, the spatial-consistency component is $O(h^4)$ and the two temporal components are $O(\tau^2)$. With the sampled initial condition $U^0 = R_h u_0$, combining this local-residual bound with Theorem 2 gives the fully discrete estimate $O(\tau^2 + h^4)$ for the exact-symbol scheme; the quadrature scheme has the additional budget E_μ. Since $\sigma > 1$ is arbitrary, one may take $\sigma = 1 + \zeta$ for any $\zeta > 0$, which requires only*

$$u_{tt} \in L^\infty(0, T; D(B^{\mu^+/2+1/2+\zeta/2})), \qquad u_{ttt} \in L^\infty(0, T; D(B^{1/2+\zeta/2})).$$

For example, choosing $\sigma = 2$, all three assumptions are implied by the stronger but simpler condition $u \in W^{3,\infty}(0, T; D(B^{\mu^+/2+2}))$. The third-order temporal regularity in $W^{3,\infty}$ is dictated by the centered-difference remainder, whose $O(\tau^2)$ bound uses u_{ttt}. The second derivative u_{tt} controls the $O(\tau^2)$ midpoint-average remainder, and the L^∞-in-time norm makes both bounds uniform over all time steps. These graph-domain hypotheses express the spectral smoothness typically associated with smooth, boundary-compatible data, with fixed-order spectral Dirichlet regularity providing the corresponding background [46]. For $\varphi(B)w = g$, the modal identity $w_{mn} = g_{mn}/\varphi(\Lambda_{mn})$ shows that the available regularity is governed by the decay of g_{mn} relative to the distributed-order symbol.

6. Numerical experiments

All experiments use $\Omega = (0,1)^2$, $\mu^- = 0.4$, $\mu^+ = 1.8$, and the uniform density $\rho(\mu) = 1$ unless otherwise stated. All tabulated spatial tests use square grids $M_x = M_y = M$, so $h = 1/M$ and $N_{\rm dof} = (M-1)^2$ on $\Omega = (0,1)^2$. The column "steps" denotes $N_t = T/\tau$. Tables 1–6 use the analytic uniform-density symbol, so $E_\mu = 0$. Table 7 studies the error introduced by positive Gauss–Legendre quadrature of the order integral, while Table 8 uses $J_\mu = 64$ only to time quadrature-based symbol precomputation. For the uniform density,

$$\varphi(s) = \frac{2(s^{\mu^+/2} - s^{\mu^-/2})}{\log s},$$

with the continuous value $\mu^+ - \mu^-$ at $s = 1$. The order interval and density are model inputs prescribed by the application, whereas h, τ, and J_μ control spatial, temporal, and order-quadrature resolution, respectively. Because the scheme is unconditionally stable, the choices $\tau = h^2/10$ in the spatial-convergence tables and $\tau = h^2/20$ in the matched comparison keep the $O(\tau^2)$ temporal error at the $O(h^4)$ spatial scale rather than imposing a stability restriction. For the smooth densities used here, J_μ is increased until successive positive-rule refinement changes the relevant operator action by less than the prescribed quadrature tolerance; this tolerance is set separately from the spatial-error target. The exact reference solution for convergence tests is the manufactured sine expansion

$$u(x,y,t) = e^{-t}\sum_{\ell=1}^{K} c_\ell \sin(k_{x,\ell}\pi x)\sin(k_{y,\ell}\pi y),$$

with the source

$$f(x,y,t) = e^{-t}\sum_{\ell=1}^{K} c_\ell \left[-1 + \varphi((k_{x,\ell}\pi)^2 + (k_{y,\ell}\pi)^2)\right] \sin(k_{x,\ell}\pi x)\sin(k_{y,\ell}\pi y).$$

The default multi-mode set is

$$(c_\ell, k_{x,\ell}, k_{y,\ell}) = (1,1,2), (0.3,4,3), (0.1,8,5).$$

The fixed high-frequency multiscale test used in Table 5 and Figure 1 is

$$(c_\ell, k_{x,\ell}, k_{y,\ell}) = (1,3,2), (0.35,7,6), (0.15,11,10).$$

All modes satisfy $k_{x,\ell}, k_{y,\ell} < 16$, so they belong to the DST-I mode set without aliasing at every reported resolution. At $M = 16$, the shortest full wavelength spans only $32/11 \approx 2.91$ grid intervals, creating the intended coarse-resolution challenge. The finite-difference comparison method uses the standard tensor-product second-order Dirichlet Laplacian:

$$A^{(2)}_{\Delta,h} = I_y \otimes T_{x,h} + T_{y,h} \otimes I_x, \qquad L^{(2)}_h = -\varphi(A^{(2)}_{\Delta,h}).$$

Its modal symbol is $\varphi(\theta_{m,x} + \theta_{n,y})$.

High-order Galerkin methods for fixed-order problems involving the spectral fractional Laplacian have also been developed and analyzed [47, 48]. For a controlled comparison under matched settings, we use the fourth-order noncompact polynomial generator

$$A^{\rm w}_{z,h} = T_{z,h} + \frac{h_z^2}{12}T^2_{z,h}, \qquad A^{\rm w}_{\Delta,h} = I_y \otimes A^{\rm w}_{x,h} + A^{\rm w}_{y,h} \otimes I_x.$$

The DST-I eigenvectors are unchanged and, for each fixed sine mode,

$$a^{\mathrm{w}}_{m,z} = \theta_{m,z}\left(1 + \frac{h_z^2}{12}\theta_{m,z}\right) = \kappa^2_{m,z} - \frac{h_z^4\kappa^6_{m,z}}{90} + O(h_z^6\kappa^8_{m,z}), \qquad \psi^{\mathrm{w}}_{mn} = \varphi\Big(a^{\mathrm{w}}_{m,x} + a^{\mathrm{w}}_{n,y}\Big).$$

Thus, the comparator is fourth order for the sine-compatible data used here, and the compact, noncompact, and second-order schemes use the same grid, distributed-order symbol, Crank–Nicolson update, time-step rule $\tau = h^2/20$, continuous $L^2(\Omega)$ error measure, and $(M-1)^2$ spatial degrees of freedom. Errors are evaluated against the exact sine-series solution.

6.1. Operator consistency

Table 1 tests, at $t = 0.3$, the operator-level defect

$$\left\|R_h\varphi(B)u - \varphi(A^{(4)}_{\Delta,h})R_hu\right\|_h.$$

For consecutive mesh sizes $h_{i-1} > h_i$, the rate in each error column is computed as $\mathrm{rate}_i = \log(E_{i-1}/E_i)/\log(h_{i-1}/h_i)$, where E_i denotes the corresponding discrete L^2 error at h_i. The compact functional-calculus operator exhibits fourth-order spatial accuracy, while the second-order full-spectral counterpart exhibits second-order spatial accuracy.

Table 1. Spatial consistency of the compact full-spectral functional-calculus operator at $t = 0.3$ for the multi-mode test, using the analytic uniform-density symbol $\mu \in [0.4, 1.8]$.

M	h	Compact error	Rate	Second-order error	Rate
16	0.06250	7.647×10^{-2}	–	6.175×10^{-1}	–
24	0.04167	1.457×10^{-2}	4.088	2.827×10^{-1}	1.927
32	0.03125	4.539×10^{-3}	4.055	1.607×10^{-1}	1.964
48	0.02083	8.859×10^{-4}	4.030	7.193×10^{-2}	1.982
64	0.01562	2.791×10^{-4}	4.015	4.057×10^{-2}	1.991
96	0.01042	5.494×10^{-5}	4.008	1.806×10^{-2}	1.995
128	0.00781	1.737×10^{-5}	4.004	1.017×10^{-2}	1.998
192	0.00521	3.427×10^{-6}	4.002	4.521×10^{-3}	1.999

6.2. Fully discrete and temporal convergence

For the manufactured solution, Table 2 directly compares the computed solution U^{N_t} with the sampled analytical solution $R_hu(T)$ by reporting $\left\|e^{N_t}\right\|_h$ and the grid maximum error $\left\|e^{N_t}\right\|_{\infty,h} := \max_{1\le i,j\le M-1}|e^{N_t}_{ij}|$, where $e^{N_t} = R_hu(T) - U^{N_t}$. Since $\tau = h^2/10$ gives $\tau^2 = h^4/100$, the temporal and spatial terms have the same fourth-order scaling in h; the factor $1/100$ affects only the constant. The observed rates are fourth order.

Table 2. Direct analytical–numerical comparison and fully discrete convergence of the unsplit modal CN compact scheme with $T = 0.2$, analytic uniform-density symbol $\mu \in [0.4, 1.8]$ so $E_\mu = 0$, and $\tau = h^2/10$. The listed rates are based on $\|e^{N_t}\|_h$.

M	h	τ	Steps	$\|e^{N_t}\|_h$	Rate	$\|e^{N_t}\|_{\infty,h}$
16	0.06250	3.906×10^{-4}	512	6.719×10^{-4}	–	1.483×10^{-3}
24	0.04167	1.736×10^{-4}	1152	1.265×10^{-4}	4.118	2.536×10^{-4}
32	0.03125	9.766×10^{-5}	2048	3.934×10^{-5}	4.061	8.717×10^{-5}
48	0.02083	4.340×10^{-5}	4608	7.673×10^{-6}	4.031	1.702×10^{-5}
64	0.01562	2.441×10^{-5}	8192	2.417×10^{-6}	4.015	5.361×10^{-6}
96	0.01042	1.085×10^{-5}	18432	4.759×10^{-7}	4.008	1.056×10^{-6}

Table 3 fixes a fine mesh and varies τ. The observed rates are consistent with the second-order convergence of the unsplit modal CN time discretization.

Table 3. Temporal convergence of the unsplit modal CN scheme on a fixed fine mesh ($M = 384$, $T = 0.32$) using the analytic uniform-density symbol, so $E_\mu = 0$.

τ	Steps	$\|e^{N_t}\|_h$	Rate
8.000×10^{-2}	4	3.150×10^{-4}	–
4.000×10^{-2}	8	7.882×10^{-5}	1.999
2.000×10^{-2}	16	1.969×10^{-5}	2.001
1.000×10^{-2}	32	4.921×10^{-6}	2.000
5.000×10^{-3}	64	1.230×10^{-6}	2.000
2.500×10^{-3}	128	3.073×10^{-7}	2.001

Table 4 repeats the compact fully discrete convergence test for several uniform distributed-order intervals. These cases examine the persistence of the fourth-order spatial trend across different order ranges.

Table 4. Compact fully discrete convergence for different uniform distributed-order intervals ($T = 0.2$, $\tau = h^2/10$, analytic symbols, $E_\mu = 0$).

$[\mu^-, \mu^+]$	M	h	τ	$\|e^{N_t}\|_h$	Rate
$[0.2, 0.8]$	24	0.04167	1.736×10^{-4}	2.871×10^{-5}	–
$[0.2, 0.8]$	32	0.03125	9.766×10^{-5}	8.936×10^{-6}	4.057
$[0.2, 0.8]$	48	0.02083	4.340×10^{-5}	1.744×10^{-6}	4.030
$[0.2, 0.8]$	64	0.01562	2.441×10^{-5}	5.492×10^{-7}	4.015
$[0.4, 1.8]$	24	0.04167	1.736×10^{-4}	1.265×10^{-4}	–
$[0.4, 1.8]$	32	0.03125	9.766×10^{-5}	3.934×10^{-5}	4.061
$[0.4, 1.8]$	48	0.02083	4.340×10^{-5}	7.673×10^{-6}	4.031
$[0.4, 1.8]$	64	0.01562	2.441×10^{-5}	2.417×10^{-6}	4.015
$[1.0, 2.0]$	24	0.04167	1.736×10^{-4}	1.446×10^{-4}	–
$[1.0, 2.0]$	32	0.03125	9.766×10^{-5}	4.496×10^{-5}	4.061
$[1.0, 2.0]$	48	0.02083	4.340×10^{-5}	8.770×10^{-6}	4.031
$[1.0, 2.0]$	64	0.01562	2.441×10^{-5}	2.763×10^{-6}	4.015

6.3. High-order comparison on a multiscale challenge

Table 5 compares the three schemes on the fixed high-frequency multiscale test. Both high-order schemes exhibit fourth-order convergence, while the compact error is smaller at every reported resolution, with a noncompact-to-compact error ratio of approximately 1.79–2.65. Because the two high-order schemes share the same DST-I basis and $O(N_{\text{dof}} \log N_{\text{dof}})$ modal-update complexity, the comparison shows the compact scheme's accuracy gain at matched asymptotic cost on this test. Figure 1 displays the corresponding continuous $L^2(\Omega)$ error curves.

Table 5. Matched accuracy comparison on the fixed high-frequency multiscale test defined in Section 6. All three grid schemes use the same $(M-1)^2$ spatial degrees of freedom, distributed-order symbol, Crank–Nicolson update, and continuous $L^2(\Omega)$ error measure ($T = 0.2$, $\tau = h^2/20$).

M	h	Compact fourth order		Noncompact fourth order		Second order	
		Error	Rate	Error	Rate	Error	Rate
16	0.06250	4.616×10^{-3}	–	8.262×10^{-3}	–	2.719×10^{-2}	–
24	0.04167	8.338×10^{-4}	4.220	1.812×10^{-3}	3.741	1.126×10^{-2}	2.174
32	0.03125	2.557×10^{-4}	4.109	6.037×10^{-4}	3.821	6.187×10^{-3}	2.081
48	0.02083	4.938×10^{-5}	4.055	1.245×10^{-4}	3.895	2.706×10^{-3}	2.040
64	0.01562	1.550×10^{-5}	4.027	4.002×10^{-5}	3.943	1.513×10^{-3}	2.019
96	0.01042	3.045×10^{-6}	4.014	8.002×10^{-6}	3.970	6.700×10^{-4}	2.010
128	0.00781	9.615×10^{-7}	4.007	2.543×10^{-6}	3.985	3.763×10^{-4}	2.005

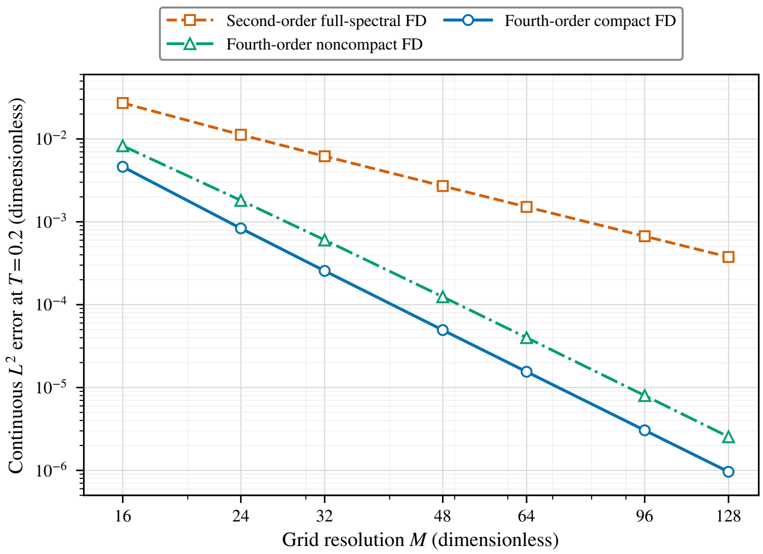

Figure 1. Continuous $L^2(\Omega)$ errors of the compact, fourth-order noncompact polynomial-generator, and second-order full-spectral schemes on the fixed high-frequency multiscale test. All schemes use the same $(M-1)^2$ spatial degrees of freedom, distributed-order symbol, and Crank–Nicolson discretization ($T = 0.2$, $\tau = h^2/20$).

6.4. Large time-step stability

For the homogeneous problem $f = 0$ with random modal initial data, Table 6 reports the discrete L^2 norms $\|U^0\|_h$, $\|U^{N_t}\|_h$, and $\max_{0\le n\le N_t}\|U^n\|_h$, whereas Figure 2 shows the normalized histories $\|U^n\|_h / \|U^0\|_h$. The norm is nonincreasing for all tested time steps. The numerical solution decays slowly for large time steps because the CN scheme is A-stable but not L-stable; this is consistent with $|G_{mn}| \le 1$.

Table 6. Discrete L^2-stability test for large time steps ($M = 128$, $T = 1$, analytic uniform-density symbol, random modal data with seed 20260524).

τ	Steps	Initial norm	Final norm	Max norm	Monotone
1.000×10^{-3}	1000	9.872×10^{-1}	8.703×10^{-7}	9.872×10^{-1}	yes
1.000×10^{-2}	100	9.872×10^{-1}	3.597×10^{-3}	9.872×10^{-1}	yes
5.000×10^{-2}	20	9.872×10^{-1}	6.752×10^{-1}	9.872×10^{-1}	yes
1.000×10^{-1}	10	9.872×10^{-1}	8.797×10^{-1}	9.872×10^{-1}	yes
5.000×10^{-1}	2	9.872×10^{-1}	9.813×10^{-1}	9.872×10^{-1}	yes
1.000×10^{0}	1	9.872×10^{-1}	9.856×10^{-1}	9.872×10^{-1}	yes

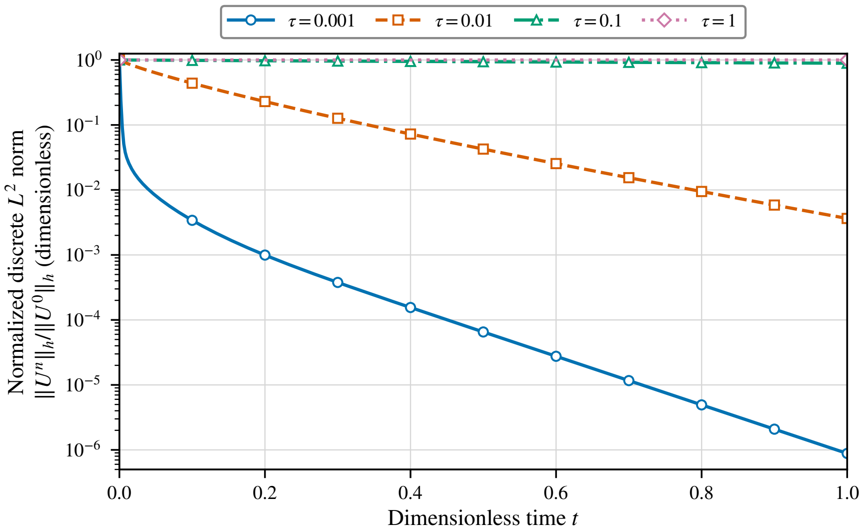

Figure 2. Normalized discrete L^2-norm histories for the homogeneous equation ($M = 128$, $T = 1$, random modal initial data, seed 20260524).

6.5. Order quadrature and implementation scaling

Table 7 reports the absolute and relative operator error introduced by positive Gauss–Legendre quadrature of the distributed-order integral. For a quadrature rule with symbol φ_J, the reported absolute error is

$$\left\|\left(\varphi_J(A^{(4)}_{\Delta,h}) - \varphi_{\mathrm{ref}}(A^{(4)}_{\Delta,h})\right) R_h v\right\|_h$$

and the relative error is obtained by dividing by $\left\|\varphi_{\mathrm{ref}}(A^{(4)}_{\Delta,h}) R_h v\right\|_h$. For the uniform density, φ_{ref} is the analytic symbol. For the endpoint-peaked density, the reference uses $J_{\mathrm{ref}} = 1024$. The high-mode operator test uses

$$v(x, y) = \sum_{\ell=1}^{5} c_\ell \sin(k_{x,\ell}\pi x) \sin(k_{y,\ell}\pi y),$$

with

$$(c_\ell, k_{x,\ell}, k_{y,\ell}) = (1, 1, 2), (0.25, 8, 7), (0.12, 16, 13), (0.06, 24, 21), (0.03, 31, 28).$$

For the endpoint-peaked case, the unnormalized density is

$$\rho_{\mathrm{ep}}(\mu) = \frac{1}{\sqrt{(\mu - \mu^- + \varepsilon)(\mu^+ - \mu + \varepsilon)}}, \qquad \varepsilon = 10^{-3}.$$

Here $\varepsilon = 10^{-3}$ defines the bounded endpoint-peaked test density; refining the high-mode reference from $J_{\mathrm{ref}} = 512$ to $J_{\mathrm{ref}} = 1024$ produces a relative change of 3.35×10^{-13} in the reference operator action, supporting $J_{\mathrm{ref}} = 1024$ at the precision reported in Table 7. The endpoint concentration slows order-quadrature convergence relative to the uniform case, so the contribution E_μ is reported separately from the h^4 spatial term. Under Assumptions 1 and 2, modal positivity gives unconditional discrete L^2 stability for admissible densities and positive rules. Accuracy at fixed J_μ is density-dependent: the uniform case reaches the roundoff level by $J_\mu = 12$, whereas endpoint concentration may require a larger or adaptive J_μ to meet the same tolerance (Table 7).

Table 7. Sensitivity to positive Gauss–Legendre quadrature of the distributed-order integral ($M = 128$, high-mode operator test and endpoint-peaked density defined in Section 6, $J_{\mathrm{ref}} = 1024$ for endpoint-peaked density; the uniform-density reference uses the analytic symbol).

Density	J_μ	Error vs. ref.	Relative error	Ref. norm
uniform	4	2.286×10^{-2}	4.873×10^{-4}	4.691×10^{1}
uniform	8	2.327×10^{-9}	4.961×10^{-11}	4.691×10^{1}
uniform	12	3.985×10^{-14}	8.496×10^{-16}	4.691×10^{1}
uniform	16	3.782×10^{-14}	8.063×10^{-16}	4.691×10^{1}
uniform	24	3.567×10^{-14}	7.605×10^{-16}	4.691×10^{1}
uniform	32	3.655×10^{-14}	7.793×10^{-16}	4.691×10^{1}
uniform	48	3.068×10^{-13}	6.541×10^{-15}	4.691×10^{1}
uniform	64	2.561×10^{-14}	5.460×10^{-16}	4.691×10^{1}
endpoint-peaked	4	3.101×10^{1}	2.164×10^{-1}	1.433×10^{2}
endpoint-peaked	8	1.202×10^{1}	8.387×10^{-2}	1.433×10^{2}
endpoint-peaked	12	6.047×10^{0}	4.221×10^{-2}	1.433×10^{2}
endpoint-peaked	16	3.351×10^{0}	2.339×10^{-2}	1.433×10^{2}
endpoint-peaked	24	1.163×10^{0}	8.114×10^{-3}	1.433×10^{2}
endpoint-peaked	32	4.330×10^{-1}	3.022×10^{-3}	1.433×10^{2}
endpoint-peaked	48	6.517×10^{-2}	4.549×10^{-4}	1.433×10^{2}
endpoint-peaked	64	1.031×10^{-2}	7.197×10^{-5}	1.433×10^{2}

Table 8 reports median wall-clock timings and the observed scaling of the modal implementation; absolute values are platform-dependent. On the square grids used here, the full-spectral symbol is stored as the two-dimensional array $\varphi(a_{m,x}^{(4)} + a_{n,y}^{(4)})$. The column "Pre. ms" reports quadrature-based symbol precomputation with $J_\mu = 64$, "DST+IDST ms" reports one forward two-dimensional DST followed by one inverse transform, and "Upd. ms" reports the modal multiplication update. The idealized working storage estimate is

$$\frac{5N_{\mathrm{dof}} \cdot 8}{10^6}\ \mathrm{MB},$$

corresponding to five double-precision arrays of length N_{dof}. The dense baseline is

$$\frac{N_{\mathrm{dof}}^2 \cdot 8}{10^9}\ \mathrm{GB},$$

the storage required by one dense $N_{\mathrm{dof}} \times N_{\mathrm{dof}}$ double-precision matrix. Thus, precomputation scales as $O(J_\mu N_{\mathrm{dof}})$, while each time step remains transform-dominated.

Table 8. Scaling diagnostic of the DST-based full-spectral modal implementation (median wall-clock timings; 20 repetitions for symbol precomputation and DST+IDST timings, and 100 repetitions for modal updates).

M	N_{dof}	J_μ	Pre. ms	DST+IDST ms	Upd. ms	Work MB	Dense GB
64	3969	64	2.78	0.05	0.003	0.2	0.1
128	16,129	64	9.36	0.16	0.008	0.6	2.1
256	65,025	64	35.03	0.74	0.034	2.6	33.8
384	146,689	64	79.84	2.67	0.167	5.9	172.1

Accuracy-matched solver comparison. To distinguish spatial-discretization accuracy from matrix-function solver cost, we additionally compare the direct DST realization with a per-step single-vector rational Krylov realization using Zolotarev poles and precomputed shifted SuperLU factorizations [49]. Both solvers use the same fourth-order compact operator, $J_\mu = 64$, and the same 100-step CN recurrence with $T = 0.2$ and $\tau = 0.002$. The initial state is the high-frequency packet defined above and the time-dependent source is

$$f_G(x, y, t) = \sin(\pi x)\sin(\pi y)\left\{e^{-70[(x-c_x(t))^2+(y-c_y(t))^2]} + 0.25\cos\left(\frac{4\pi t}{T}\right)e^{-45[(x-0.72)^2+(y-0.28)^2]}\right\},$$

where $c_x(t) = 0.35 + 0.12\sin(2\pi t/T)$ and $c_y(t) = 0.58 + 0.10\cos(2\pi t/T)$. For each grid, the selected number of poles k satisfies

$$\varepsilon_{\mathrm{traj}} := \max_{1\le n\le 100} \frac{\|U^n_{\mathrm{RK}} - U^n_{\mathrm{DST}}\|_h}{\|U^n_{\mathrm{DST}}\|_h} \le 10^{-8}.$$

Table 9 reports a controlled single-threaded benchmark on an Intel Core Ultra 7 265K: timings are medians of five 100-step runs, the online denominator is a conservative physical-space direct-DST update at each step, and peak working-set ratios are medians from five fresh processes per method. At matched discrete accuracy, the tested rational Krylov realization uses 33–123 times the setup time, 36–138 times the online time, and 1.16–3.80 times the gross peak working set of direct DST. This solver-level comparison is limited to the specified realization and the separable setting, whereas Table 5 compares spatial accuracy.

Table 9. Accuracy-matched solver-level comparison for the same fourth-order compact operator and CN recurrence. The setup and online columns are rational-Krylov/direct-DST time ratios. The last column is the ratio of median gross process peak working sets.

M	N_{dof}	Poles k	$\varepsilon_{\mathrm{traj}}$	Setup ratio	100-step ratio	Peak RSS ratio
32	961	11	9.88×10^{-9}	33	36	1.16
64	3969	14	3.79×10^{-9}	72	94	1.62
96	9025	15	5.00×10^{-9}	97	119	2.49
128	16,129	16	4.41×10^{-9}	123	138	3.80

7. Conclusions

We have developed a fourth-order compact functional-calculus method for full-spectral distributed-order diffusion on rectangular Dirichlet domains. The compact Kronecker-sum generator $A^{(4)}_{\Delta,h}$ serves as the discrete counterpart of $B = -\Delta_D$, and the distributed-order symbol is applied directly to this generator,

$$\Phi_h = \varphi(A^{(4)}_{\Delta,h}), \qquad L_h = -\Phi_h.$$

The resulting method is unsplit: each modal Crank–Nicolson step uses the full two-dimensional compact eigenvalue rather than a product of directional factors. The analysis shows that the compact eigenvalue perturbation is preserved by φ, giving a fourth-order discrete L^2 consistency estimate for $\varphi(B)$ after grid restriction. Positivity of the exact symbol, and of the positive quadrature rules used for the order integral, gives dissipativity and unconditional discrete L^2 stability. Under the stated regularity assumptions, the fully discrete error is $O(\tau^2 + h^4)$ for the exact-symbol scheme and $O(\tau^2 + h^4 + E_\mu)$ for the positive-quadrature version.

The numerical experiments support these conclusions through operator-level tests, fully discrete and temporal convergence studies, order-interval checks, stability histories, quadrature sensitivity tests, and a comparison with the second-order full-spectral counterpart. The results show the expected fourth-order spatial accuracy, second-order temporal accuracy, nonincreasing discrete L^2 norms for the homogeneous problem, and the separate effect of the quadrature budget.

The present analysis relies on rectangular separability, homogeneous Dirichlet data, quasi-uniform tensor-product grids, and sine-diagonalizable full-spectral operators. The rectangular geometry, homogeneous Dirichlet data, and a tensor-product grid that is uniform in each coordinate direction provide the DST-I basis that simultaneously diagonalizes $A^{(4)}_{\Delta,h}$ and $\varphi(A^{(4)}_{\Delta,h})$; without this separable structure, neither the present modal fourth-order transfer proof nor the $O(N_{\mathrm{dof}} \log N_{\mathrm{dof}})$ DST implementation carries over directly. The numerical study is limited to smooth finite sine-series data on uniform square grids. Future work should address nonrectangular geometries, nonhomogeneous boundary data, nonuniform meshes, numerical validation of the regularity–rate tradeoff in Corollary 1, nonlinear extensions, and adaptive positive order-quadrature rules for endpoint-concentrated densities.

Author contributions

Xiaotong Li: Methodology, Software, Validation, Formal analysis, Writing–original draft; Jianxin Li: Conceptualization, Methodology, Supervision, Writing–review and editing. All authors have read and approved the final version of the manuscript for publication.

Use of Generative-AI tools declaration

The authors used OpenAI only for English language and grammar checking during manuscript preparation. The authors take full responsibility for the content of this article.

Data availability statement

No external datasets were used. The numerical data supporting the tables and figures are available from the corresponding author upon reasonable request.

Acknowledgments

This work was supported by the President's Fund of Xinjiang University of Political Science and Law (Grant No. XZZK2025014). The funder had no role in the study design, generation of numerical results, analysis, interpretation, manuscript preparation, or the decision to submit the article for publication.

Conflict of interest

The authors declare no conflicts of interest.

References

1. R. L. Bagley, P. J. Torvik, On the existence of the order domain and the solution of distributed order equations–Part I, *International Journal of Applied Mathematics*, **2** (2000), 865–882.
2. R. L. Bagley, P. J. Torvik, On the existence of the order domain and the solution of distributed order equations–Part II, *International Journal of Applied Mathematics*, **2** (2000), 965–987.
3. M. Caputo, Distributed order differential equations modelling dielectric induction and diffusion, *Fract. Calc. Appl. Anal.*, **4** (2001), 421–442.
4. A. V. Chechkin, R. Gorenflo, I. M. Sokolov, Retarding subdiffusion and accelerating superdiffusion governed by distributed-order fractional diffusion equations, *Phys. Rev. E*, **66** (2002), 046129. https://doi.org/10.1103/PhysRevE.66.046129
5. W. Ding, S. Patnaik, S. Sidhardh, F. Semperlotti, Applications of distributed-order fractional operators: A review, *Entropy*, **23** (2021), 110. https://doi.org/10.3390/e23010110
6. K. Diethelm, N. J. Ford, Numerical analysis for distributed-order differential equations, *J. Comput. Appl. Math.*, **225** (2009), 96–104. https://doi.org/10.1016/j.cam.2008.07.018
7. G.-H. Gao, H.-W. Sun, Z.-Z. Sun, Some high-order difference schemes for the distributed-order differential equations, *J. Comput. Phys.*, **298** (2015), 337–359. https://doi.org/10.1016/j.jcp.2015.05.047

8. E. Kharazmi, M. Zayernouri, G. E. Karniadakis, Petrov–Galerkin and spectral collocation methods for distributed order differential equations, *SIAM J. Sci. Comput.*, **39** (2017), A1003–A1037. https://doi.org/10.1137/16M1073121
9. M. A. Zaky, J. T. Machado, Multi-dimensional spectral tau methods for distributed-order fractional diffusion equations, *Comput. Math. Appl.*, **79** (2020), 476–488. https://doi.org/10.1016/j.camwa.2019.07.008
10. N. J. Higham, *Functions of matrices: theory and computation*, Philadelphia: SIAM, 2008. https://doi.org/10.1137/1.9780898717778
11. A. Bonito, J. E. Pasciak, Numerical approximation of fractional powers of elliptic operators, *Math. Comp.*, **84** (2015), 2083–2110. https://doi.org/10.1090/S0025-5718-2015-02937-8
12. A. Lischke, G. F. Pang, M. Gulian, F. Y. Song, C. Glusa, X. N. Zheng, et al., What is the fractional Laplacian? A comparative review with new results, *J. Comput. Phys.*, **404** (2020), 109009. https://doi.org/10.1016/j.jcp.2019.109009
13. S. K. Lele, Compact finite difference schemes with spectral-like resolution, *J. Comput. Phys.*, **103** (1992), 16–42. https://doi.org/10.1016/0021-9991(92)90324-R
14. J. C. Strikwerda, *Finite difference schemes and partial differential equations*, 2 Eds., Philadelphia: SIAM, 2004. https://doi.org/10.1137/1.9780898717938
15. D. W. Peaceman, H. H. Rachford, The numerical solution of parabolic and elliptic differential equations, *J. Soc. Indust. Appl. Math.*, **3** (1955), 28–41. https://doi.org/10.1137/0103003
16. J. Douglas, On the numerical integration of $u_{xx} + u_{yy} = u_t$ by implicit methods, *J. Soc. Indust. Appl. Math.*, **3** (1955), 42–65. https://doi.org/10.1137/0103004
17. J. Douglas, J. E. Gunn, A general formulation of alternating direction methods, *Numer. Math.*, **6** (1964), 428–453. https://doi.org/10.1007/BF01386093
18. F. H. Zeng, F. W. Liu, C. P. Li, K. Burrage, I. Turner, V. Anh, A Crank–Nicolson ADI spectral method for a two-dimensional Riesz space fractional nonlinear reaction-diffusion equation, *SIAM J. Numer. Anal.*, **52** (2014), 2599–2622. https://doi.org/10.1137/130934192
19. H. Zhang, F. W. Liu, X. Y. Jiang, F. H. Zeng, I. Turner, A Crank–Nicolson ADI Galerkin–Legendre spectral method for the two-dimensional Riesz space distributed-order advection-diffusion equation, *Comput. Math. Appl.*, **76** (2018), 2460–2476. https://doi.org/10.1016/j.camwa.2018.08.042
20. R. M. Hafez, Y. H. Youssri, R. Hafez, Exponential/fractional Jacobi spectral Galerkin and collocation schemes for the multi-dimensional time-fractional diffusion equations on the semi-infinite domain, *Hacet. J. Math. Stat.*, **55** (2026), 942–961.
21. Z. D. Abbasov, G. Albeladi, M. Gamal, Y. H. Youssri, Analytical and numerical analysis of multidimensional diffusion processes in L^2 space under third-kind boundary conditions, *Axioms*, **15** (2026), 380. https://doi.org/10.3390/axioms15050380
22. S. G. Kamel, A. G. Atta, Y. H. Youssri, An explicit spectral Tau method with Delannoy polynomials for the time-fractional diffusion equation, *Open Journal of Mathematical Analysis*, **9** (2025), 134–144. https://doi.org/10.30538/psrp-oma2025.0169

23. W. M. Abd-Elhameed, Y. H. Youssri, A. G. Atta, Adopted spectral tau approach for the time-fractional diffusion equation via seventh-kind Chebyshev polynomials, *Bound. Value Probl.*, **2024** (2024), 102. https://doi.org/10.1186/s13661-024-01907-6
24. M. H. Salama, H. A. Zedan, W. M. Abd-Elhameed, Y. H. Youssri, A spectrally accurate shifted Lucas collocation framework for fractional Lanchester combat dynamics with time-dependent variable coefficients, *J. Comput. Appl. Mech.*, **57** (2026), 425–442. https://doi.org/10.22059/jcamech.2026.412544.1799
25. Y. Yang, J. Huang, Double fast algorithm for solving time-space fractional diffusion problems with spectral fractional Laplacian, *Appl. Math. Comput.*, **475** (2024), 128715. https://doi.org/10.1016/j.amc.2024.128715
26. K. Kazmi, A fast and high-order IMEX method for non-linear time-space-fractional reaction-diffusion equations, *Numer. Algor.*, **95** (2024), 243–266. https://doi.org/10.1007/s11075-023-01570-5
27. K. Kazmi, A. Q. M. Khaliq, An efficient split-step method for distributed-order space-fractional reaction-diffusion equations with time-dependent boundary conditions, *Appl. Numer. Math.*, **147** (2020), 142–160. https://doi.org/10.1016/j.apnum.2019.08.019
28. M. Abbaszadeh, M. Dehghan, alternating direction implicit (ADI) finite difference scheme for solving the two-dimensional distributed-order Riesz space-fractional diffusion equation, *Appl. Numer. Math.*, **158** (2020), 271–291. https://doi.org/10.1016/j.apnum.2020.07.020
29. X. J. Chen, J. H. Chen, F. W. Liu, Z.-Z. Sun, A fourth-order accurate numerical method for the distributed-order Riesz space fractional diffusion equation, *Numer. Meth. Part. D. E.*, **39** (2023), 1266–1286. https://doi.org/10.1002/num.22933
30. H. S. Bauomy, Active control impact analysis on shaped coupled beam structure, *AIMS Math.*, **10** (2025), 30732–30772. https://doi.org/10.3934/math.20251349
31. H. S. Bauomy, A. T. EL-Sayed, Oscillation controlling in nonlinear motorcycle scheme with bifurcation study, *Mathematics*, **13** (2025), 3120. https://doi.org/10.3390/math13193120
32. H. S. B. Abdelmonem, Dual nonlinear saturation control of electromagnetic suspension (EMS) system in maglev trains, *Mathematics*, **14** (2026), 62. https://doi.org/10.3390/math14010062
33. H. S. Bauomy, Advanced vibrant controller results of an energetic framework structure, *Open Eng.*, **14** (2024), 20240055. https://doi.org/10.1515/eng-2024-0055
34. F. Mainardi, A. Mura, G. Pagnini, R. Gorenflo, Time-fractional diffusion of distributed order, *J. Vib. Control*, **14** (2008), 1267–1290. https://doi.org/10.1177/1077546307087452
35. M. Ilić, I. W. Turner, V. Anh, A numerical solution using an adaptively preconditioned Lanczos method for a class of linear systems related with the fractional Poisson equation, *International Journal of Stochastic Analysis*, **2008** (2008), 104525. https://doi.org/10.1155/2008/104525
36. R. L. Schilling, R. M. Song, Z. Vondraček, *Bernstein functions: theory and applications*, Berlin: De Gruyter, 2010. https://doi.org/10.1515/9783110215311
37. N. Hale, N. J. Higham, L. N. Trefethen, Computing A^{α}, $\log(A)$, and related matrix functions by contour integrals, *SIAM J. Numer. Anal.*, **46** (2008), 2505–2523. https://doi.org/10.1137/070700607

38. A. Bonito, W. Y. Lei, J. E. Pasciak, Numerical approximation of the integral fractional Laplacian, *Numer. Math.*, **142** (2019), 235–278. https://doi.org/10.1007/s00211-019-01025-x
39. M. Benzi, I. Simunec, Rational Krylov methods for fractional diffusion problems on graphs, *BIT Numer. Math.*, **62** (2022), 357–385. https://doi.org/10.1007/s10543-021-00881-0
40. L. N. Trefethen, *Spectral methods in MATLAB*, Philadelphia: SIAM, 2000. https://doi.org/10.1137/1.9780898719598
41. C. Canuto, M. Y. Hussaini, A. Quarteroni, T. A. Zang, *Spectral methods: fundamentals in single domains*, Berlin: Springer, 2006. https://doi.org/10.1007/978-3-540-30726-6
42. W. Hundsdorfer, J. Verwer, *Numerical solution of time-dependent advection-diffusion-reaction equations*, Berlin: Springer, 2003. https://doi.org/10.1007/978-3-662-09017-6
43. M. H. Derakhshan, Stability analysis of difference-Legendre spectral method for two-dimensional Riesz space distributed-order diffusion-wave model, *Comput. Math. Appl.*, **144** (2023), 150–163. https://doi.org/10.1016/j.camwa.2023.05.035
44. C. Engström, S. Giani, L. Grubišić, Numerical solution of distributed-order time-fractional diffusion-wave equations using Laplace transforms, *J. Comput. Appl. Math.*, **425** (2023), 115035. https://doi.org/10.1016/j.cam.2022.115035
45. Y. Kumar, P. Yadav, V. K. Singh, Distributed order Gauss–Quadrature scheme for distributed order fractional sub-diffusion model, *Chaos Soliton. Fract.*, **170** (2023), 113358. https://doi.org/10.1016/j.chaos.2023.113358
46. G. Grubb, Regularity of spectral fractional Dirichlet and Neumann problems, *Math. Nachr.*, **289** (2016), 831–844. https://doi.org/10.1002/mana.201500041
47. C. T. Sheng, D. Cao, J. Shen, Efficient spectral methods for PDEs with spectral fractional Laplacian, *J. Sci. Comput.*, **88** (2021), 4. https://doi.org/10.1007/s10915-021-01491-2
48. Y. M. Zhang, Y. Li, Y. X. Yu, W. S. Wang, Error estimates of general linear and spectral Galerkin methods for the fractional diffusion equation with spectral fractional Laplacian, *Comp. Appl. Math.*, **44** (2025), 157. https://doi.org/10.1007/s40314-025-03116-y
49. T. Danczul, C. Hofreither, J. Schöberl, A unified rational Krylov method for elliptic and parabolic fractional diffusion problems, *Numer. Linear Algebr.*, **30** (2023), e2488. https://doi.org/10.1002/nla.2488

A. Sine sampling and aliasing

We record the aliasing estimate used in Lemmas 4 and 6. The sine-series aliasing identities used below are standard in pseudospectral collocation and spectral methods [40, 41]. It is enough to prove the estimates for finite sine expansions and then pass to the stated graph-norm spaces by completion. Write

$$w = \sum_{m,n\geq 1} w_{mn} e_{mn}.$$

For each resolved pair $1 \leq p \leq M_x - 1$, $1 \leq q \leq M_y - 1$, define the two-dimensional sine alias class

$$C_{pq} = \{(m,n) \in \mathbb{N}^2 : m \equiv \pm p \pmod{2M_x},\ n \equiv \pm q \pmod{2M_y}\}.$$

Modes with an index that is a multiple of M_x or M_y vanish on the corresponding grid and do not enter the sampled coefficients. The signs in the aliasing formula are those induced by sine symmetry.

With the orthonormal DST-I normalization used in the paper,

$$\widetilde{w}_{pq} := (h_x h_y)^{1/2}(\widehat{R_h w})_{pq} = \sum_{(m,n)\in C_{pq}} \eta_{mn,pq} w_{mn}, \qquad \eta_{mn,pq} \in \{-1, 1\}.$$

For $\beta \geq 0$ and $\sigma > 1$, the Cauchy–Schwarz inequality gives

$$\begin{aligned}\Lambda_{pq}^{\beta}|\widetilde{w}_{pq}|^2 &\leq \left(\sum_{(m,n)\in C_{pq}} \Lambda_{mn}^{-\sigma}\right)\left(\sum_{(m,n)\in C_{pq}} \Lambda_{pq}^{\beta}\Lambda_{mn}^{\sigma}|w_{mn}|^2\right)\\ &\leq C \sum_{(m,n)\in C_{pq}} \Lambda_{mn}^{\beta+\sigma}|w_{mn}|^2.\end{aligned}$$

Here $\Lambda_{pq} \leq C\Lambda_{mn}$ on each alias class. For $j \geq 1$, let

$$S_j = \{(m,n) \in \mathbb{N}^2 : \max\{m,n\} = j\}.$$

Then $|S_j| = 2j - 1$ and $j^2 \leq m^2 + n^2 \leq 2j^2$ on S_j. Since $\Lambda_{mn} \geq c_\Omega(m^2 + n^2)$ on the fixed rectangle, the integral test gives

$$\begin{aligned}\sup_{p,q} \sum_{(m,n)\in C_{pq}} \Lambda_{mn}^{-\sigma} &\leq C_{\Omega,\sigma} \sum_{m,n\geq 1} (m^2+n^2)^{-\sigma}\\ &\leq 2C_{\Omega,\sigma}\sum_{j=1}^{\infty} j^{1-2\sigma} \leq 2C_{\Omega,\sigma}\left(1 + \int_1^{\infty} r^{1-2\sigma}\,\mathrm{d}r\right) < \infty, \qquad \sigma > 1.\end{aligned}$$

At $\sigma = 1$, the unresolved sublattice $(2\ell M_x + 1, 2kM_y + 1) \in C_{11}$, $\ell, k \geq 1$, has $\Lambda_{2\ell M_x+1,\,2kM_y+1} \leq Ch^{-2}(\ell^2 + k^2)$; hence $\sum_{(m,n)\in C_{11}} \Lambda_{mn}^{-1} \geq ch^2 \sum_{\ell,k\geq 1}(\ell^2 + k^2)^{-1} = \infty$. Thus both alias sums diverge logarithmically at the endpoint. The preceding upper bound is uniform in p, q, and h. Summing over p, q and using the finite overlap of the alias classes yields

$$h_x h_y \sum_{p,q} \Lambda_{pq}^{\beta}|(\widehat{R_h w})_{pq}|^2 \leq C \sum_{m,n\geq 1} \Lambda_{mn}^{\beta+\sigma}|w_{mn}|^2.$$

This proves the weighted trace bound in Lemma 4; the unweighted trace bound is the case where $\beta = 0$.

For the unresolved tail, replace C_{pq} by $C_{pq}^H = C_{pq} \setminus \{(p,q)\}$. Every mode in C_{pq}^H has at least one index bounded below by a positive multiple of M_x or M_y. More explicitly, the positive representatives in an alias class have the form $|2\ell M_x \pm p|$ and $|2kM_y \pm q|$. After removing (p,q), at least one of $|\ell|$ or $|k|$ is nonzero. Hence

$$\Lambda_{mn} \geq ch^{-2}(\ell^2 + k^2),$$

apart from harmless changes in the constant caused by the finitely many sign choices. Since $\sum_{(\ell,k)\neq(0,0)}(\ell^2 + k^2)^{-r} < \infty$ for $r > 1$, we obtain

$$\sup_{p,q} \sum_{(m,n)\in C_{pq}^H} \Lambda_{mn}^{-r} \leq Ch^{2r}, \qquad r > 1,$$

where $h = \max\{h_x, h_y\}$. Applying the same Cauchy–Schwarz argument to the unresolved alias classes gives

$$\|R_h(I - \Pi_h)w\|_h^2 \leq Ch^{2r} \sum_{m,n\geq 1} \Lambda_{mn}^r |w_{mn}|^2,$$

and therefore,

$$\|R_h(I - \Pi_h)w\|_h \leq Ch^r \left\|B^{r/2}w\right\|_{L^2}, \qquad r > 1.$$